Available online at www.sciencedirect.com
ScienceDirect
International Journal of Heat and Mass Transfer 50 (2007) 1455–1468
International Journal of HEAT and MASS TRANSFER
www.elsevier.com/locate/ijhmt

On the influence of pore shape, contact angle and film flows on drying of capillary porous media

M. Prat *

Institut de Mécanique des Fluides de Toulouse, UMR CNRS – INP/UPS No. 5502, Avenue du professeur Camille Soula, 31400 Toulouse, France

Received 13 January 2006; received in revised form 7 September 2006
Available online 17 November 2006

Abstract

As pointed out in several previous works, thick liquid film flow can represent a major transport mechanism in drying. The effect of films is to greatly reduce the drying time compared to situations where they cannot develop. Using pore network simulations, we explore the influence of pore shape and contact angle on drying rates during the isothermal drying of porous materials in relation with the effect of liquid films when viscous effects are important in the films but not in the liquid saturated pores. It is shown that the overall drying time is greatly affected by the pore shape and contact angle when film flows are important and that incorporating the film effect in the pore network model leads to a much better agreement with experimental results. Film flows can significantly contribute to the occurrence and/or the duration of the constant rate period (CRP), which is a classical feature of convective drying. When film flows are important, the quantitative prediction of drying rate becomes very difficult for it depends on tiny details of the pore space geometry and is affected by possible changes in the local wettability conditions. This contributes to explain why the accurate prediction of drying rate still remains essentially an open question, at least when the effect of films cannot be neglected.

Keywords: Drying; Pore network; Film flow; Corner flow

1. Introduction

Drying of porous media has been the subject of many studies and is still a very active research topic. In addition to its practical importance in relation with the industrial drying of many products, drying can still be considered as an unsolved problem from a scientific standpoint. For example the quantitative prediction of drying rate without any parameter calibration is still essentially an open problem. In this paper, we try to shed some light into this problem with the analysis of the influence of film flows, pore shape and contact angle on drying rates. We begin with capillary tubes of polygonal cross-section and then consider a pore network model with pores of polygonal cross-section. Pore-network models for the study of drying have been used for more than 10 years, e.g. [1] and references therein. A pore network model for studying drying patterns and drying rates was first proposed in [2] for slow evaporation of a single component liquid when thermal effects can be ignored. This two-dimensional model takes into account capillary effects through an invasion percolation (IP) rule and the transport by diffusion in the gas phase of the evaporating species. Since this first attempt, increasingly sophisticated models have been developed so as to take into account gravity effects [3], viscous effects [4], thermal effects [5,6], film effects [7,8], binary liquids [9]. Three dimensional versions, though not including all effects, have also been developed [10–12]. Experiments with etched networks [13] have led to satisfactory comparisons in terms of drying patterns and have shown the strong influence of film flows on drying rates [14]. The analysis of drying patterns can be performed using invasion percolation concepts and this has been performed in some details in [15,16], notably in relation with the experimental results reported in [17] indicating that the viscous effects stabilize

* Tel.: +33 05 61 28 58 83; fax: +33 05 61 28 58 99.
E-mail address: prat@imft.fr

0017-9310/$ - see front matter © 2006 Elsevier Ltd. All rights reserved.
doi:10.1016/j.ijheatmasstransfer.2006.09.001

Nomenclature

A	cross-section area, m^2
c	vapor mass fraction, kg/kg
c_e	equilibrium vapor mass fraction, kg/kg
c_i	vapor mass fraction at the interface, kg/kg
c_∞	vapor mass fraction in surrounding air, kg/kg
$\bar{c}$	cross-section averaged mass fraction, kg/kg
Ca	capillary number
D	vapor diffusion coefficient, m^2/s
e	evaporation flux density, $kg/m^2/s$
E	evaporation flux, kg/s
E_{ref}	reference evaporation flux, kg/s
f	dimensionless factor
F	cluster mass flux, kg/s
h	dimensionless mass transfer coefficient
g	gravity acceleration, m/s/s
ℓ	diffusion screening length, m
k	permeability, m^2
L	tube or porous medium length, m
N	number of tube sides
p	pressure, Pa
p_g	gas pressure, Pa
p_{cth}	threshold capillary pressure, Pa
P	wetted perimeter, m
q_m	mass flow rate, kg/s
Q_{ev}	evaporation source term, kg/m/s
R	curvature radius, m
R_0	tube size, m
S	overall liquid saturation
t	time, s
t_c	time at which sub-regime 2 starts, s
y	corner meniscus curvature radius, m
z	coordinates, m
z_c	bulk meniscus position at $t = t_c$, m
z_f	film tip position, m
z_0	position of bulk meniscus, m
Δc	$c_e - c_\infty$, kg/kg
α	half angle
β	dimensionless resistance factor
δ	external transfer length scale, m
ε	porosity
γ	surface tension, N/m
κ	dimensionless parameter
λ	dimensionless factor = 3.77
η	dimensionless factor
ϕ	composite variable
θ	equilibrium contact angle
θ_c	critical contact angle
μ	dynamic viscosity, Pl
ψ_i, $i = 1,2,3,4$	numerical factors
ρ_g	gas phase density, kg/m^3
ρ_l	liquid phase density, kg/m^3
τ	reference time, s
χ	dimensionless curvature

the invasion. More recently, pore network models have been used to study the influence of pore size distributions on saturation and transport parameters as well as on drying kinetics [11,18,19].

As mentioned before we concentrate in this paper on the influence of pore shape and contact angle on drying rates. More specifically, we consider three basic pore shapes, i.e. triangular, square and hexagonal and show that the pore shape and the contact angle can greatly affect the drying kinetics. This is first shown for a simple bundle of capillary tubes and then with pore networks. Note however that we restrict our attention to situations where the liquid is always the wetting fluid and the invasion percolation algorithm can be applied to determine which bond is to be invaded in each cluster present in the network. For example, the case of hydrophobic networks is not considered. The pore network model used in this study is an extension of the model proposed in [2] so as to include the transport in liquid phase by the pore corner films. For modelling the transport in the film region and dry region of network, the method is essentially the one proposed by Yiotis et al. [7]. In addition to the pore shape and the influence of contact angle the main difference lies in the boundary condition at the open edge of network with the introduction of an external boundary layer characteristic size (instead of a Dirichlet condition). The paper is organized as follows. In the next section we study the influence of shape and contact angle on evaporation kinetics for a bundle of non-interconnected capillary tubes. Section 3 deals with the case of pore networks. In Section 4 we discuss the results, notably in relation with the classical description of drying kinetics in several periods, e.g. [20].

2. Evaporation from capillary tubes of polygonal cross-section

Evaporation driven by mass transfer has been studied experimentally in microchannels of rectangular cross-section [21], as well as in capillary tubes of square cross-section [22]. These works indicate that evaporation in channels with corners is much faster than in a channel of circular cross-section. This is attributed to the effects of liquid films developing along the channel corners. Because of these films, the modelling of evaporation in a channel of polygonal cross-section is significantly more complex than for a circular tube. A model of liquid flow with evaporation in a channel of square cross-section in relation with the modelling of drying of porous media was presented in [7]. Various evaporation regimes can be distinguished in a tube of polygonal cross-section depending on the competition

between capillary, viscous and gravity forces [23,24]. For square tubes, the regime dominated by the capillary forces was studied in [23] and a modelling for the various regimes was presented in [24]. In the present paper, we concentrate on the capillary-viscous regime, i.e. gravity effect are negligible, and extend the modelling to tubes of triangular and hexagonal cross-section. Also, the modelling takes into account the effect of the contact angle.

2.1. Modelling of evaporation in polygonal capillaries

We consider the convective evaporation of a bundle of vertical capillary tubes initially saturated by a pure liquid. A representative tube of this model porous medium is depicted in Fig. 1 in the case of a square tube. Evaporation takes place due to the gas flow along the capillary entrance. The other end of capillary is sealed. Owing to convective flow, mass and momentum boundary layers form along the tube entrance. A rough approximation of the boundary layer effect is to assume that the external transfer occurs through a diffusive layer of uniform thickness δ. Thus δ is the characteristic length scale of external transfer. Under these circumstances, the evaporation flux density e at the surface is given by

$$e = \rho_g D \frac{(c_i - c_\infty)}{\delta} \tag{1}$$

where D, ρ_g, c_i, c_∞ are the diffusion coefficient of water vapour, gas phase density, water vapour mass fraction at the porous medium surface and water vapour mass fraction in the free stream respectively. It is interesting to estimate orders of magnitude of δ. Typically, at temperatures close to 20 °C, e is the range 10^{-4}–10^{-3} kg/m^2/s for a drying porous medium. This corresponds to δ in the range 10^{-4}–10^{-3} m (we have taken $D = 2.5 \times 10^{-5}$ m^2/s, $\rho_g = 1.19$ kg/m^3, $c_i = 0.0144$, $c_\infty = 0$). These values are representative of porous media (≈periodic array of tubes). For a single tube δ can be much lower. As the motivation is the study of drying of porous media δ will be kept constant, regardless of the tube size. Thus, in this paper, the capillary tube should be considered as a unit tube of a spatially periodic array of tubes.

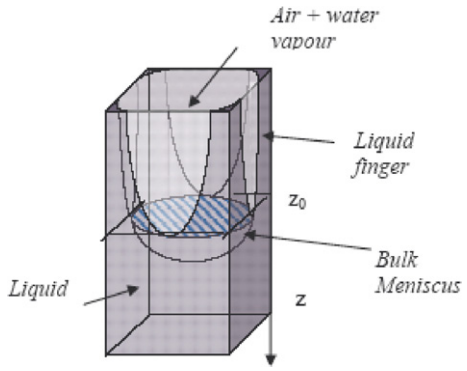

Fig. 1. Schematic of drying of a square capillary.

Determining the evolution of meniscus position z_0 and evaporation rate e is a classical problem when the capillary cross-section is circular [25]. In the dilute limit, the solutions read

$$z_0 = \sqrt{\frac{2\rho_g D \Delta c}{\rho_l} t + \delta^2} - \delta \tag{2}$$

$$e = \frac{\rho_g D \Delta c}{\sqrt{\frac{2\rho_g D \Delta c}{\rho_l} t + \delta^2}} \tag{3}$$

where $\Delta c = c_e - c_\infty$. Hence z_0 scales as $\sqrt{t}$ for a circular tube. Compared to polygonal tubes Eqs. (2) and (3) represent lower bounds.

As mentioned above, the evolution can be expected to be drastically different when the tube is of polygonal cross-section owing to the liquid flow along the tube edges induced by the capillary forces. In what follows, we consider the cases of capillaries of square, triangular and hexagonal cross-section as depicted in Fig. 2. We assume that the liquid is wetting with θ as receding equilibrium contact angle. We study evaporation at the ambient temperature for a not too volatile fluid, e.g. water. Under these circumstances, evaporation is driven by mass transfer and temperature variations can be ignored.

As in drainage in a polygonal capillary [26], evaporation is characterized by the invasion of the tube bulk by the gas phase and, when the contact angle is lower than a critical value, the presence of liquid "fingers" trapped by capillarity within the corners of the tube as sketched in Fig. 1. The critical contact angle θ_c depends on the tube shape and is simply given by $\theta_c = \pi/N$ where N is the number of tube sides, i.e. $N = 3, 4, 6$ for triangular, square and hexagonal tubes, respectively. Thus, corner flows cannot exist for $\theta \geqslant 60°$ in a triangular tube, $\theta \geqslant 45°$ for a square one and $\theta \geqslant 30°$ for a hexagonal one.

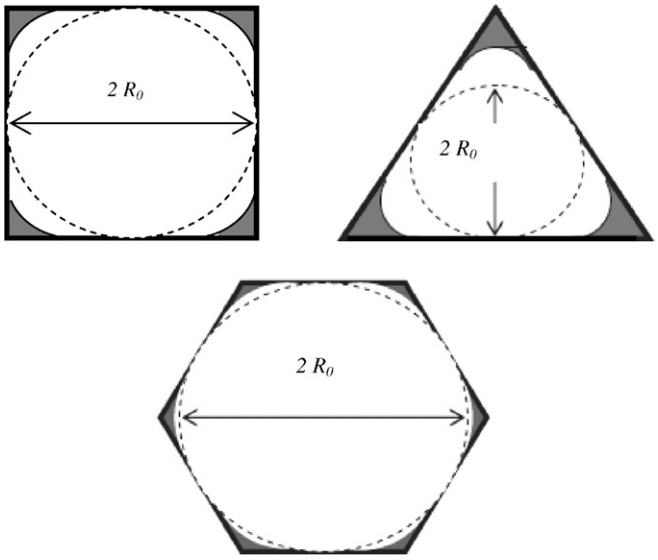

Fig. 2. The three pore shapes considered.

Let R be the liquid /gas interface curvature radius in the tube cross-section in the corner film region. According to [26] an upper limit R_{th} for R, corresponding to a corner finger whose shape only depends on capillary forces, can be deduced from the equation,

$$p_{cth} = \frac{\gamma}{R_{th}} = \frac{\gamma\chi}{R_0} \tag{4}$$

where R_0 is the radius of the largest inscribed sphere in the capillary and γ is the surface tension. According to [27], the dimensionless curvature χ can be expressed as a function of θ and θ_c as

$$\chi = \cos\theta + [(\theta_c - \theta + \sin\theta\cos\theta)/\tan\theta_c]^{1/2} \tag{5}$$

As $\chi > 1$ when $\theta \leqslant \theta_c$, $R_{th} < R_0$. Hence the liquid wedges in corners only wet a fraction of tube walls. The tube wall region between the liquid fingers can be carpeted by very thin liquid films whose thickness is of the order of a few nanometers. These liquid films can be neglected for tubes with size much greater than the film thickness [5]. Another issue is the shape of the liquid wedge right at the entrance of the tube, where the curvature of the wedge liquid gas interface in the z-direction is not negligible. Actually, the experimental results reported in Camassel [22] suggest that the evaporation rate is dependent on the details of phenomena occurring in the tube tip region, i.e. the evaporation rate is deemed to depend on the local properties of tube edges at the entrance such as roughness, small cracks, wetting properties. This renders difficult accurate quantitative predictions of evaporation rate when the liquid wedges reach the tube entrance, which is not the objective of the present paper. As a result, since the details are generally not known, we have adopted the rather crude model in which the wedge interface curvature along the z-direction is neglected right from the entrance. This should not change the overall qualitative picture described in this paper, that is essentially the qualitative influence of tube shape and contact angle on evaporation.

Detailed 3D simulations of evaporation for this crude model have been performed [5]. The results of these simulations have been shown to be in good agreement with a simplified 1D model [23]. This simplified model, which is used in the present paper, is obtained from considering the cross-section averaged water vapour fraction $\bar{c}$. The transport equation for the vapor within the tube reads

$$\frac{\partial}{\partial z}\left(\rho_g(A_t - A_c)D\frac{\partial\bar{c}}{\partial z}\right) + Q_{ev} = 0 \tag{6}$$

where A_t and A_c are the tube cross-section area and corner area, respectively. A_t can be expressed as a function of R_0 with $A_t = \pi R_0^2 + NR_0^2\left(\cot\alpha - \frac{\pi}{2} + \alpha\right)$, where α is the half-angle of the corner ($\alpha = 30°$, $45°$ and $60°$ for the triangular, square and hexagonal tubes, respectively). Thus $A_t = 3\sqrt{3}R_0^2$ for the triangular tube, $A_t = 4R_0^2$ for the square one and $A_t = 2\sqrt{3}R_0^2$ for the hexagonal one. A_c, which is the sum of liquid corner area and round corner area [28,29] can be expressed as

$$A_c = NR^2\left[\frac{\cos\theta}{\sin\alpha}\cos(\alpha+\theta) - \frac{\pi}{2} + \alpha + \theta\right] = NR^2\psi_4 \tag{7}$$

with $\psi_4 = \left[\frac{\cos\theta}{\sin\alpha}\cos(\alpha+\theta) - \frac{\pi}{2} + \alpha + \theta\right]$.

The boundary conditions are expressed as

$$\rho_g(A_t - A_c)D\frac{\partial\bar{c}}{\partial z} = \rho_g(A_t - A_c)D\frac{(\bar{c} - c_\infty)}{\delta} \quad \text{at } z = 0 \tag{8}$$

$$\bar{c} = c_e \quad \text{at } z = z_0 \tag{9}$$

where z_0 is the position of the bulk meniscus within the tube.

In Eq. (6), the source term Q_{ev}, which represents the internal evaporation at the liquid finger surface, is simply expressed as $Q_{ev} = \rho_g hPD\frac{(c_e - \bar{c})}{R_0}$ where P is the wetted perimeter, which is given by $P = 2NR\left(\frac{\pi}{2} - \alpha - \theta\right)$. The mass transfer coefficient h can be regarded as a fitting parameter. It can be determined by comparison with 3D simulation results, e.g. [23]. However, this parameter needs not to be analysed in detail here since its influence can be in fact neglected when $R_0 \ll \delta$ as it is considered in the following.

In this model, the total evaporation flux is given by

$$E = \rho_g A_l D\frac{\Delta c}{\delta} + \rho_g(A_t - A_c)D\frac{(\bar{c}(0) - c_\infty)}{\delta} \tag{10}$$

where A_l is the liquid corner area; $A_l = A_c - NR^2r^2[\cot\alpha - \pi/2 + \alpha]$ where $r = r_0/R$, r_0 is the radius of the round corner (for the sake of generality we assume for the moment that the corner is not perfectly sharp and that the tip of the corner possesses a certain degree of roundedness characterized by r_0, see [28,29] for more details).

The evolution of the bulk meniscus location as a function of time is deduced from the simple mass balance,

$$\rho_l(A_t - A_c(z_0))\frac{dz_0}{dt} = E \tag{11}$$

where $A_c(z_0)$ is given by Eq. (7) with $R = R_{th}$. In what follows, this model is combined with a model describing the evolution of the liquid wedge shape.

2.1.1. Liquid mass balance in fingers

Under the assumption of a quasi-steady state, e.g. [7], the mass balance in liquid wedges read

$$\frac{\partial q_m}{\partial z} = Q_{ev} \quad 0 \leqslant z \leqslant z_0 \tag{12}$$

in which q_m is the mass flow rate in the fingers. The boundary conditions associated with Eq. (12) are expressed as

$$q_m = -\rho_g A_l D\frac{\Delta c}{\delta} \quad \text{at } z = 0 \tag{13}$$

$$q_m = -E \quad \text{at } z = z_0 \tag{14}$$

As shown in [28], the mass flow rate in the N corners can be expressed as

$$q_m = -\rho_l\frac{A_c R^2}{\beta\mu}\frac{dp}{dz} \quad 0 \leqslant z \leqslant z_0 \tag{15}$$

where μ and ρ_l are the liquid viscosity and density respectively; β is a dimensionless resistance depending on the shape of the corner and the boundary condition at the liquid–air interface. According to [29], for a free boundary condition at the liquid–gas interface, β can be estimated as

$$\beta = \frac{12\sin^2\alpha(1-B)^2}{(1-\sin\alpha)^2 B^2}\frac{(\psi_1 - B\psi_2)(\psi_3-(1-B)r)^2}{(\psi_1 - B\psi_2 - (1-B)r^2)^3} \tag{16}$$

where $\psi_1 = \cos^2(\alpha+\theta) + \cos(\alpha+\theta)\sin(\alpha+\theta)\tan\alpha$, $B = (\pi/2-\alpha)\tan\alpha$, $\psi_2 = 1 - \frac{\theta}{\pi/2-\alpha}$, $\psi_3 = \cos(\alpha+\theta)/\cos\alpha$.

With the assumption of a very large radius of curvature in the plane parallel to the axis z, the pressure in the corner is linked to the surface tension γ and R by Laplace's law,

$$p = p_g - \frac{\gamma}{R(z)} \tag{17}$$

As the gas pressure p_g is constant, combining Eqs. (12)–(17) leads to

$$\frac{d}{dz}\left[\frac{N\rho_l\kappa\gamma R^2}{\mu}\frac{dR}{dz}\right] = -Q_{ev} \tag{18}$$

where $\kappa = \psi_4/\beta$ and with $R = R_{th}$ at $z = z_0$.

As discussed in [23,24,7], the concentration $\bar{c}$ follows an exponential decay within a region of a few film thickness at the tip of the film. Also, we are interested in situations where the "pore" size R_0 is small compared to the external boundary layer thickness δ, i.e. $R_0 \ll \delta$. Under these circumstances, a reasonable approximation is to consider $\bar{c} \approx c_e$ when a film is present. This leads to $Q_{ev} \approx 0$ and

$$\frac{N\rho_l\kappa\gamma R^2}{\mu}\frac{dR}{dz} = E \approx \rho_g A_f D\frac{\Delta c}{\delta + z_f} \tag{19}$$

where $A_f = A_t + A - A_c$ and $R = R_{th}$ at $z = z_0$. In Eq. (19), z_f is the position of the films tip within the tube.

Choosing R_0 as characteristic length and c_e as reference concentration, Eq. (19) is expressed in dimensionless form as

$$\frac{dR^{*3}}{dz^*} = \frac{fCa}{\delta^* + z_f^*} \tag{20}$$

where $f = \frac{A_f^*}{N\kappa}$ the capillary number Ca is defined by $Ca = \frac{3\mu\rho_g D\Delta c}{\rho_l R_0 \gamma}$ and $R^* = \chi^{-1}$ at $z^* = z_0^*$.

Using $\tau = \frac{\rho_l R_0^2}{\rho_g D\Delta c}$ as characteristic time, Eq. (11) is expressed in dimensionless form as

$$\frac{dz_0^*}{dt^*} = \frac{A^{*-1}}{\delta^* + z_f^*} \tag{21}$$

where $A^* = (A_t - A_c(z_0))/A_f$.

Two main sub-regimes can be distinguished depending on the position of film tip. The first sub-regime is when the film is present up to the entrance of the tube, i.e. $z_f^* = 0$.

2.1.2. Sub-regime 1 (film tip at the tube entrance)

From Eqs. (20) and (21) with $z_f^* = 0$. we obtain,

$$R^*(0)^3 = \chi^{-3} - fCa\frac{z_0^*}{\delta^*} \tag{22}$$

and

$$z_0^* = A^{-1}\frac{t^*}{\delta^*} \tag{23}$$

Hence this analysis suggests that $z_0 \propto t$ in this regime.

This regime lasts until $R^*(0) \approx 0$, that is when

$$z_0^* = z_{0c}^* \approx f^{-1}Ca^{-1}\delta^*\chi^{-3} \tag{24}$$

which corresponds to time t_c^* given by

$$t_c^* \approx \delta^* z_{0c}^* = Af^{-1}Ca^{-1}\chi^{-3}\delta^{*2} \tag{25}$$

2.1.3. Sub-regime 2 (receding film tip)

At $t = t_c$, the second regime starts. The film tip recedes within the tube. From Eq. (22), we get

$$z_f^* = \frac{z_0^*\chi^3 fCa - \delta^*}{\chi^3 fCa + 1} \tag{26}$$

The evolution of the bulk meniscus is deduced from Eq. (21) and is given by

$$z_0^* = \sqrt{2A^{-1}(1+\chi^{-3}f^{-1}Ca^{-1})(t^* - t_c^*) + (z_{0c}^* + \delta^*)^2} - \delta^* \tag{27}$$

Interestingly, Eq. (27) indicates that z_0 should scale as $\sqrt{t}$ when the viscous effects are sufficient for $z_{0c} < L$, where L is the tube length.

The tube drying time t_D, which is defined as the time when the bulk meniscus reaches the tube end, i.e. when $z_0 = L$, reads

$$t_D^* = \frac{A}{2(1+f^{-1}Ca^{-1}\chi^{-3})}[L^{*2} + 2\delta^* L^* + Ca^{-2}f^{-2}\chi^{-6}\delta^{*2}] \tag{28}$$

Naturally, when $z_{0c} > L$, the sub-regime 2 cannot be seen. This corresponds to the capillary regime. As discussed in [23,24], the drying rate is constant in this regime, see Eq. (23), and independent of the tube shape.

2.2. Influence of pore shape, contact angle, boundary layer thickness and Ca

The influence of tube shape and contact angle on drying time is explored in this section. We consider water at 20 °C as working fluid, $c_\infty = 0$, and takes $\delta = 5\times10^{-4}$ m as characteristic thickness of the external boundary layer. As a representative example, computations have been made for $L = 0.4$ m and the inscribed sphere radius $R_0 = 5$ μm. Perfectly sharp corners are assumed throughout the remaining of the paper, so that $r = 0$. This leads to $Ca = 3.6\times10^{-6}$. In passing, it is interesting to note that the roundedness of the corner does affect the flow

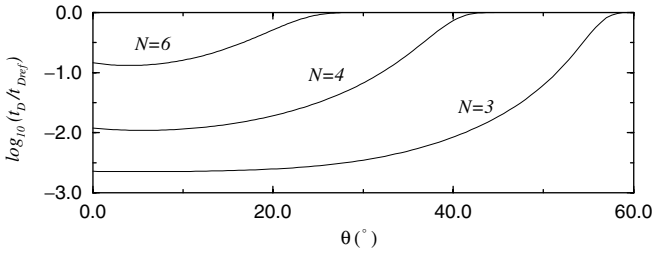

Fig. 3. Evolution of drying time as a function of contact angle for the three tube shapes.

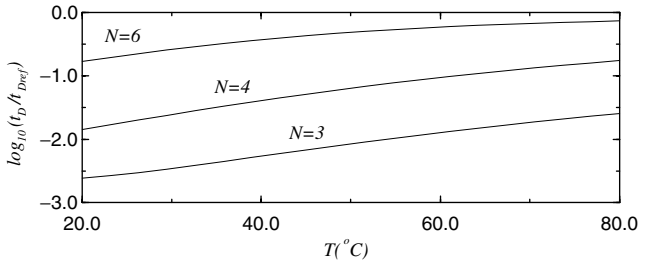

Fig. 5. Evolution of t_D/t_{Dref} as a function of the average temperature T.

resistance in the film, Eq. (16), see [28] for more details. Therefore this "detail" of the pore geometry should also affect the evaporation rate.

Fig. 3 shows the evolution of drying time as a function of contact angle for the three tube shapes. The reference time t_{Dref} in Fig. 3 is the drying time for a circular tube. This is also the drying time for tubes of polygonal cross-section when $\theta \geqslant \theta_c$. As can be seen from Fig. 3, the pore shape can greatly influence the drying time with drying times that can vary over more than two decades depending on the pore shape. For a given contact angle, the drying time significantly increases with N.

Also Fig. 3 indicates that an identical overall drying time can be obtained for quite different systems. For instance, a triangular tube with $\theta = 52°$, a square one with $\theta = 33°$ and a hexagonal one with $\theta = 0°$ lead in this example to the same overall drying time. It is therefore interesting to explore whether these different systems can be discriminated from simple experiments. As illustrated in Fig. 4 which shows the evolution of drying rate $\frac{dz_0^*}{dt^*}/\frac{dz_0^*}{dt^*}\Big|_{t^*=0}$ as a function of $(L - z_0)/L$, i.e. $\approx$ the liquid saturation, the three systems lead to the same drying kinetics. This is expected since the sole parameter depending on the pore structure and contact angle in the model is $f = \frac{A_f^*}{N\kappa}$ and f has the same value for these three systems. We conclude that a wrong determination of contact angle can lead to a wrong conclusion regarding the pore shape of this particular porous medium from classical drying experiments.

For a given tube shape, Fig. 3 also shows that the contact angle can be a very sensitive parameter. This suggests that a modification of contact angle for a given porous medium can lead to significant different drying kinetics and illustrates the significance of film flows on drying rates.

From Eq. (26), it can be deduced that $z_0^* - z_f^* = \frac{z_0^* + \delta^*}{\chi^3 fCa + 1}$, which indicates that the film length $z_0^* - z_f^*$ is a decreasing function of Ca. As a result, the overall drying time tends toward the reference time as Ca increases. To qualitatively illustrate this effect, the ratio t_D/t_{Dref} is plotted as a function of the average temperature T in Fig. 5 for the three tube shapes and, as before, $L = 0.4$ m, $\delta = 5 \times 10^{-4}$m, $R_0 = 5$ μm, $c_\infty = 0$. To obtain the results shown in Fig. 5, we simply have varied c_e as a function of temperature for $\theta = 0$, ignoring the variations of surface tension, contact angle, densities, diffusion coefficient and viscosity as a function of temperature. Also, it can be argued that the assumption of low water vapour concentration does not hold for temperatures higher than about 30–40 °C and that the thermal gradients associated with the evaporation process are not negligible in the range of temperature considered. Taking into account all these effects would not change the qualitative picture illustrated in Fig. 5, which clearly indicates that increasing the evaporation flux reduces the film extension and thereby the influence of film flows on the drying rates.

Varying the external boundary layer thickness δ has a significant effect only in the capillary regime, i.e. when the films extend up to the tube entrance. According to Eq. (23) $\frac{dz_0}{dt} \propto \delta^{-1}$ in this regime. In the capillary viscous-regime, the influence of boundary layer thickness becomes negligible as soon as $z_f \ll \delta$, which is for example the case for the results reported in Figs. 3 and 4. Thus, when the conditions are such that the capillary-viscous regime starts from the beginning of drying (i.e. $z_{0c}/L \ll 1$), we deduce from Eq. (28) that t_D^* can be safely estimated as $t_D^* \approx \frac{AL^{*2}}{2(1+f^{-1}Ca^{-1}\chi^{-3})}$.

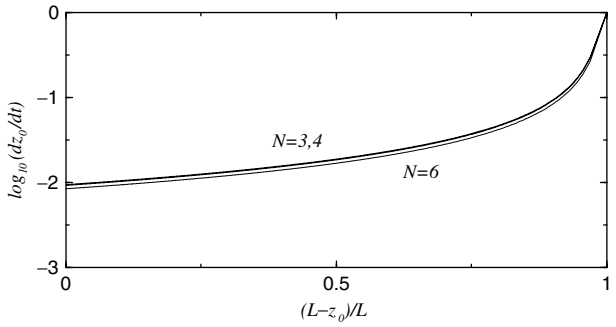

Fig. 4. Evolution of tube drying rate as a function of $(L - z_0)/L$.

3. Drying of pore networks

3.1. Pore network model of drying with film flows

As mentioned in Section 1, several pore network models of drying have been proposed in the literature. For simplicity, in this paper, we consider a single component liquid and a situation where heat transfer can be neglected. This corresponds typically to evaporation of a not too volatile liquid at the ambient temperature. The pore space is

conceptualized as a network of randomly sized pores (sites) joined by randomly sized throats (bonds). As in many previous works, a square lattice is used in this paper. The bonds are straight channels of polygonal cross-section and characterized by the radius R_0 of largest inscribed sphere. For simplicity, R_0 is distributed according to an uniform distribution law in the range $[R_{0\min}, R_{0\max}]$ with $\overline{R}_0 = (R_{0\min} + R_{0\max})/2$. Three edges of network are impervious (no mass transfer at these boundaries). The vapour escapes through the remaining open edge (top edge in Fig. 6). Initially, the network is completely saturated by the liquid.

In the present study, viscous effects are taken into account in the films but not within the pores fully saturated. This is supported by the following order of magnitude analysis. Suppose the pore mean size is $\overline{R}_0$. Then, as in [16], we can express the length L_{cap} over which the pressure drop in the saturated pores due to viscous forces is comparable to the pressure difference associated with capillary effects as

$$\frac{L_{\text{cap}}}{\overline{R}_0} \approx 0.25\chi\delta^* \left(\frac{Ca}{\Sigma}\right)^{-1} \tag{29}$$

where $\Sigma = R^*_{0\max} - R^*_{0\min}$. To derive Eq. (29), we have estimate the permeability of the pore network as $k \approx \frac{\pi \overline{R}_0^2}{8}$. The length L_{cap} can be compared to the maximum extension of film z_{0c}, which is given by Eq. (24),

$$\frac{L_{\text{cap}}}{z_{0c}} \approx 0.25\Sigma f \chi^4 \tag{30}$$

As an example, for the representative data considered in Section 2.2 ($L = 0.4$ m, $\delta = 0.5 \times 10^{-4}$ m, $R_0 = 5$ μm, $c_\infty = 0$) with $\theta = 0$ and $\Sigma = 1$, one obtains $\frac{L_{\text{cap}}}{L} \approx 72$, $\frac{z_{0c}}{L} \approx 0.6$ and $\frac{L_{\text{cap}}}{z_{0c}} \approx 116$, which clearly indicates than viscous effects can be neglected in the saturated pores since $\frac{L_{\text{cap}}}{L} \gg 1$ but not in the films since $\frac{z_{0c}}{L} \ll 0.6$ except for very narrow pore size distributions, i.e. $\Sigma \leqslant 10^{-2}$.

Thus the above estimates indicate that there exist situations in which viscous effects can be neglected in the bulk but not in the film. For instance, this is the case in the pore network experiments reported in [14]. In this paper, we concentrate on this type of situation. However, it can be pointed out that we have derived the above estimates using an expression of the permeability corresponding to a saturated network. Actually, the effective permeability of the liquid phase decreases with the liquid saturation. Thus, it is expected that the viscous effects eventually become non-negligible as the liquid phase approaches the liquid phase percolation threshold. However, this effect remains marginal under the conditions and system sizes considered in the present study, that are representative of slow drying of usual capillary porous media. It is possible to develop models including viscous effects in both films and bulk as proposed by Yiotis et al. [8] but this would make the computations much more intensive without any significant change in the results, at least for the conditions and systems considered in the present paper. Again the emphasis is here on the influence of pore shape and contact angle in relation with film flow.

As first described in Prat [2], neglecting viscous effects in the saturated pores leads to apply IP rules to each cluster in order to determine which bond should be invaded in each cluster. Compared to the simple model proposed in [2], the objective is simply to take into account the transport by the films in addition to the transport by diffusion in the gas phase. As sketched in Fig. 6, we can distinguish three main regions in a drying porous medium when film flows are significant: the fully saturated regions, the dry region in which the water transport takes place by diffusion in gas phase and the film region between the saturated

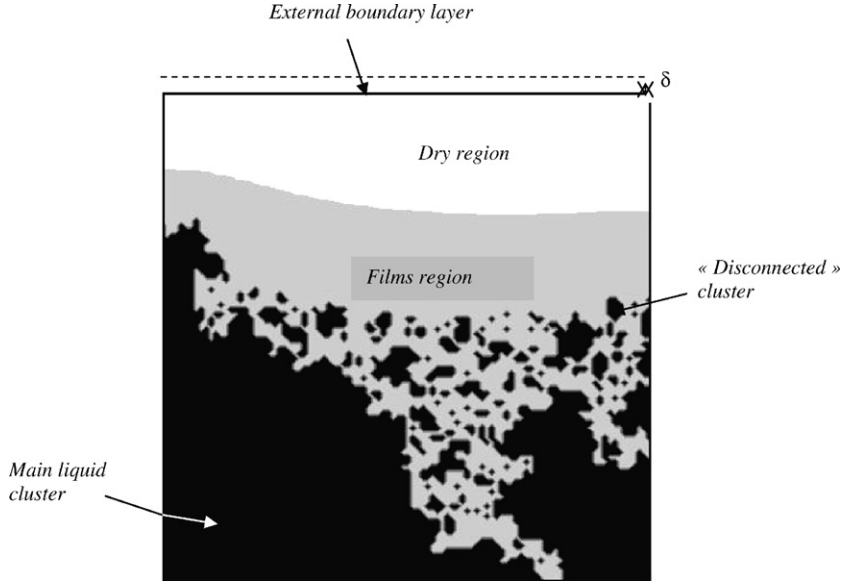

Fig. 6. Sketch of phase distribution during the drying process.

clusters and the dry region. As in the tube problem discussed in the previous section, the dry region may not develop before all clusters have been drained out. This will be discussed in more details in the following.

As for the tube problem, the transport in the dry and films regions can be considered as quasi-steady, e.g. [7]. Following [7], we assume that the film hydraulic connectivity is not too perturbed in the pores. Hence a simple extension of tube model for describing film transport within the film region of pore network reads

$$\nabla \cdot \left[\frac{N\rho_l \kappa \gamma}{3\mu} \nabla R^3 \right] = 0, \tag{31}$$

whereas the governing equation for the concentration in the dry zone reads

$$\nabla \cdot \left[\rho_g A_f D \nabla c \right] = 0, \tag{32}$$

where A_f is the cross-section area of dry bonds. Thus A_f varies with the considered bond.

At the boundary Γ_{fd} between the film region and the dry zone, the flux continuity reads

$$\frac{N\rho_l \kappa \gamma}{3\mu} \nabla R^3 \cdot \mathbf{n} = \rho_g A_f D \nabla c \cdot \mathbf{n} \quad \text{at } \Gamma_{fd} \tag{33}$$

where $\mathbf{n}$ is a unit normal vector at the film region/dry region boundary.

The expression of the boundary condition at the open edge of network varies depending on the presence or not of the film at the boundary.

$$\frac{N\rho_l \kappa \gamma}{3\mu} \frac{\partial R^3}{\partial z} = \rho_g A_f D \frac{\Delta c}{\delta} \quad \text{at } z = 0 \text{ when } R \geqslant 0 \tag{34}$$

$$\rho_g A_f D \frac{\partial c}{\partial z} = \rho_g A_f D \frac{(c - c_\infty)}{\delta} \quad \text{at } z = 0 \text{ when } R = 0 \tag{35}$$

In principle, the boundary condition at a cluster boundary Γ_{cf} is given by the size R_0 of the bond selected by the IP rule, i.e. $R = R_{th} = \frac{R_0}{\chi}$ at Γ_{cf}. However, in the present effort, we have adopted the same simplification as in [7], i.e. the film radius at the liquid clusters is constant and equal to R_c, corresponding to the percolation threshold. Thus, the boundary condition is expressed as

$$R_c = \frac{R_{0c}}{\chi} \quad \text{at } \Gamma_{cf} \tag{36}$$

where for a uniform throat size p.d.f and a square network, $R_{0c} = (R_{0\max} + R_{0\min})/2$. Although this assumption would certainly deserve to be investigated in more depth [7], this should not change the essentially qualitative findings of the present paper.

Once Eqs. (31)–(36) are solved the net drainage flux F (in kg/s) at a cluster boundary is given by

$$F = \sum_{i=1,m} \frac{N\rho_l \kappa \gamma}{3\mu} \nabla R^3 \cdot \mathbf{n}_c \tag{37}$$

where m is the number of interfacial bond forming the cluster boundary and $\mathbf{n}_c$ is the outwardly directed unit normal vector. The time needed for evaporating the volume V_l of liquid contained in the cluster invaded bond is given by

$$t_c = \frac{\rho_l V_l}{\sum_{i=1,m} \frac{N\rho_l \kappa \gamma}{3\mu} \nabla R^3 \cdot \mathbf{n}_c} \tag{38}$$

3.1.1. Method of solution

The method of solution used in the present study for solving the transport equation in the film and dry regions is essentially the one presented by Yiotis et al. [7]. The sole differences lie in the boundary conditions (34) and (35) (a Dirichlet condition is used in [7]). As for the straight tubes, it is convenient to express the above equations in dimensionless form. Under the approximation $A_f(R_0) \approx A_f(\overline{R}_0)$, choosing $\overline{R}_0$ as characteristic length and $c^* = \frac{c - c_\infty}{c_e - c_\infty}$ as dimensionless concentration lead to express Eqs. (31)–(38) in dimensionless form as

$$\Delta R^{*3} = 0 \tag{39}$$

$$\Delta c^* = 0 \tag{40}$$

$$\nabla R^{*3} \cdot \mathbf{n} = fCa \nabla c^* \cdot \mathbf{n} \quad \text{at } \Gamma_{fd} \tag{41}$$

$$\frac{\partial R^{*3}}{\partial z^*} = fCa\delta^{*-1} \quad \text{at } z^* = 0 \text{ when } R^* \geqslant 0 \tag{42}$$

$$\frac{\partial c^*}{\partial z^*} = \delta^{*-1} c^* \quad \text{at } z^* = 0 \text{ when } R^* = 0 \tag{43}$$

$$R^* = \chi^{-1} R^*_{0c} \quad \text{at } \Gamma_{cf} \tag{44}$$

Then the next step is to introduce the variable $\phi = R^{*3} + fCac^*$, which allows to express the above problem as

$$\Delta \phi = 0 \quad \text{in } \Omega_{fd} \tag{45}$$

$$\frac{\partial \phi}{\partial z^*} = fCa\delta^{*-1} \quad \text{at } z^* = 0 \text{ when } R^* \geqslant 0 \text{ i.e. when } \phi \geqslant fCa \tag{46}$$

$$\frac{\partial \phi}{\partial z^*} = \delta^{*-1} \phi \quad \text{at } z^* = 0 \text{ when } R^* = 0 \text{ i.e. when } \phi \leqslant fCa \tag{47}$$

$$\phi = fCa + \chi^{-3} R^{*3}_{0c} \quad \text{at } \Gamma_{cf} \tag{48}$$

Using $\tau = \frac{\rho_c R_0^2}{\rho_g D \Delta c}$ as characteristic time, a cluster selected bond drainage time t_c is expressed in dimensionless form as

$$t^*_c = \frac{V^*_l}{\sum_{i=1,m} Ca^{-1} f^{-1} A^*_f \nabla \phi \cdot \mathbf{n}_c} \tag{49}$$

Problem (45)–(48) is solved on the film region/dry region using a finite volume technique. The method is identical as the one used for solving the diffusion transport problem in the gas phase in the model without films, e.g. [2], and therefore the details are not presented again.

Adapting the drying algorithm of Ref. [2] is now straightforward:

(1) Every liquid cluster present in the network is identified.

(2) The bond connected to the already invaded region which has the lowest threshold capillary pressure is identified for each cluster (the threshold capillary pressure of a bond is expressed as $P_{\mathrm{cth}} = \frac{\gamma\chi}{R_0}$ where the factor χ is given by Eq. (5)), the volume of liquid contained at time t in this bond and the adjacent pore is V_{sc}.
(3) The mass flux F_{c} at the boundary of each cluster is computed from the computation of ϕ over the film region/dry region.
(4) For each cluster, the time t_{c}^{*} required to drain the amount of liquid contained in the bond identified in step (2) is computed using Eq. (49).
(5) The bond (as well as the adjacent pore) among the bonds selected in step (2) eventually invaded is that corresponding to $t_{\mathrm{c\,min}}^{*} = \min(t_{\mathrm{c}}^{*})$.
(6) The phase distribution within the network is updated, which includes the partial drainage of liquid contained in the bond bulks selected in step (2) with $\rho_{\mathrm{l}} V_{\mathrm{l}}(t + t_{\mathrm{c\,min}}) = \rho_{\mathrm{l}} V_{\mathrm{l}}(t) - F_{\mathrm{c}} t_{\mathrm{c\,min}}$ except for the bulk of bond and adjacent pore selected in step (5) which become completely drained.

3.2. Influence of pore shape and contact angle

Simulations have been carried out for 100×100 pore networks. The throat sizes are distributed randomly between 1 and 9 μm according a uniform distribution law. The distance a between two nodes of network is 1 mm. As before, we consider water at 20 °C as working fluid, $c_{\infty} = 0$, and takes $\delta = 5 \times 10^{-4}$ m as characteristic thickness of the external boundary layer. Representative examples of phase distribution evolution during drying are shown in Fig. 7. These cases correspond to the main three regimes: no film ($\theta/\theta_{\mathrm{c}} \geqslant 1$, Fig. 7c), films present up to the porous medium surface over most of drying (Fig. 7a), and the intermediate regime with films receding into the porous medium (Fig. 7b). When $\theta/\theta_{\mathrm{c}} \approx 1$, no film develops, the transport from the liquid clusters is by diffusion in the gas phase only and evaporation takes place within the network during most of drying. In the intermediate regime, films can extent over the system up to the porous medium surface over a significant period of drying. During this period, the transport from the liquid clusters up to the porous medium surface takes place through the films only and the evaporation takes place at the porous medium surface. Then, the films recede within the porous domain and a dry zone eventually develops from the porous medium surface. During the last period of drying, evaporation takes place at the boundary between the film region and the dry zone. As can be seen from Fig. 7, the phase distribution is practically not affected by the presence or not of the films. This is consistent with the experiments

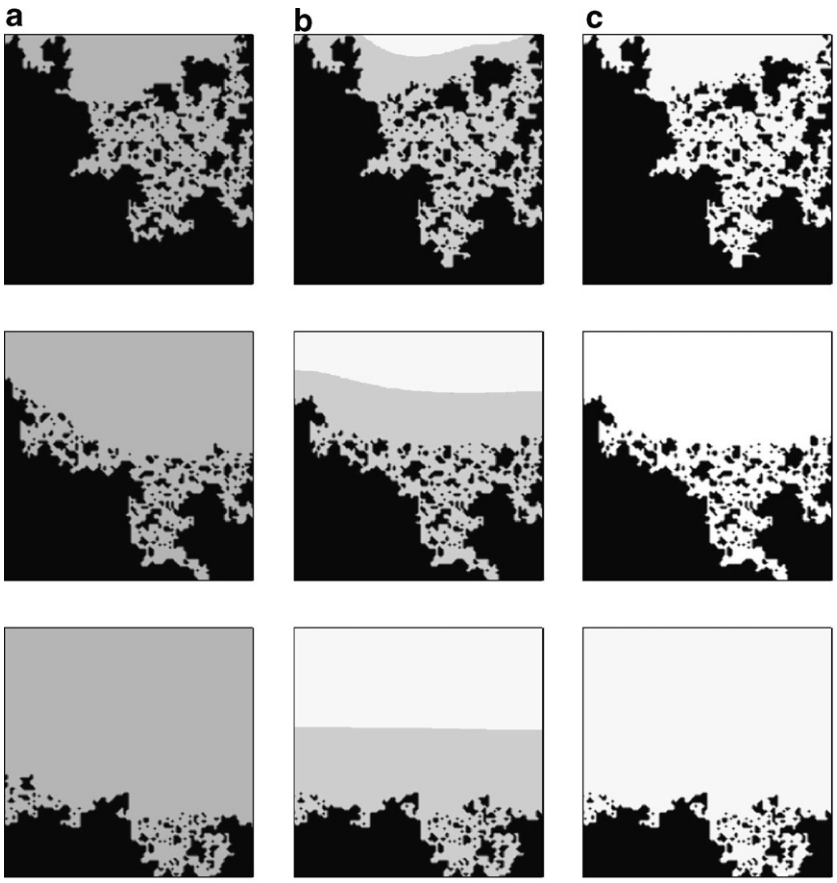

Fig. 7. Examples of phase distribution evolution during drying. Liquid saturated regions in black, dry zone in white, films region in grey. Vapour escapes from top edge. (a) Dominant film regime (sub-regime 1), (b) intermediate regime (sub-regime 2), (c) no film, $\theta \geqslant \theta_{\mathrm{c}}$.

on etched networks reported in [13]. As pointed out in [14], the films flow is expected to have a major influence on the drying rates but not much on the phase distributions, at least within the range of capillary numbers considered in the present study. Fig. 8 shows the evolution of overall liquid saturation S as a function of time for the various pore shapes and $\theta/\theta_c = 0$, $\theta/\theta_c = 0.5$ and $\theta/\theta_c \approx 1$ whereas Fig. 9 shows the evolution of drying curves. In Fig. 8, t_{θ_c} is the overall drying time for $\theta = \theta_c$, i.e. in the absence of films; $t_{\theta_c} = 5967$ h for the example considered. As expected, the films dramatically affect the drying rates. For this example, the triangular pore shapes lead to the same fast evaporation when $\theta/\theta_c = 0$ or $\theta/\theta_c = 0.5$ for films extend up to the porous surface until the end of drying. By contrast, films recede into the network for the square and hexagonal pore shape during drying leading to a slower drying. The greatest the critical contact angle θ_c, the fastest the drying when film flows are important and recede within the porous medium during drying.

3.3. Influence of external transfer

When the conditions are such that the films reach the porous surface over a significant period of drying, the system is sensitive to external drying conditions. By contrast, when a dry zone develops, the internal transport resistance due to diffusion in gas phase controls the drying rates and drying becomes essentially insensitive to change in the external transfer conditions. As long as the film reaches the interface the evolution of average saturation is readily obtained from a simple mass balance since the evaporation flux density is constant and given by

$$e_{CR} \approx \rho_g D \frac{(c_e - c_\infty)}{\delta} \tag{50}$$

Thus

$$S(t) = 1 - \frac{e_{CR}}{L\varepsilon\rho_l} t \tag{51}$$

where ε is the porous medium porosity.

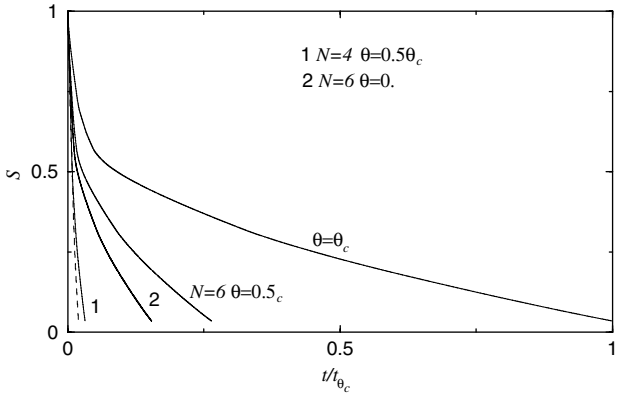

Fig. 8. Evolution of liquid overall saturation as a function of time. t_{θ_c} is the overall drying time for $\theta = \theta_c$, i.e. when film effects can be ignored. The dashed curve corresponds to the regime where films are present at the surface of network all over drying (sub-regime 1).

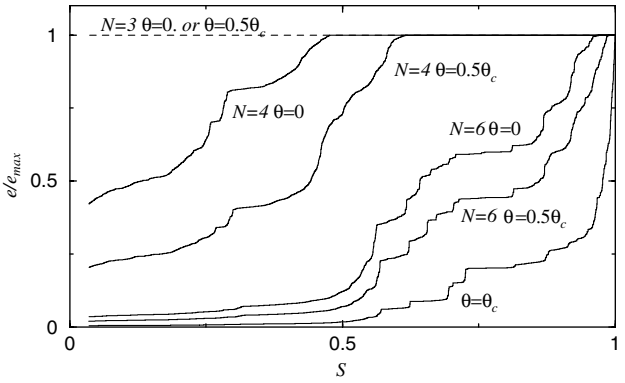

Fig. 9. Drying curves. S is the overall liquid saturation of network.

This constant rate period ends when the films begin to recede into the porous medium. From the tube analysis, we know that this approximately occurs at time t_c^* given by $t_c^* \approx \delta^* z_{0c}^* = Af^{-1}Ca^{-1}\chi^{-3}\delta^{*2}$ when the liquid cluster effective boundary is at $z_0^* = z_{0c}^* \approx f^{-1}Ca^{-1}\delta^*\chi^{-3}$. Therefore, we expect that the critical saturation S_c marking the end of constant rate period approximately scales as $1 - S_c \propto \delta$. As shown in Fig. 10, this is only a rough scaling since the boundary of the film region is not a straight line parallel to the surface of the porous medium in general (see Fig. 7). When the conditions are such that the films reach the porous medium surface during the whole drying process, the overall drying time is simply given by $t_D \approx \frac{L\varepsilon\rho_l\delta}{\rho_g D\Delta c}$ and therefore directly scales as δ. From boundary layer theory, we therefore expect in this case that $t_D \propto U_\infty^{-m}$, where U_∞ is the velocity of the external flow and $m = 4/5$ for a turbulent flow.

3.4. Comparison with experiments

An important and interesting question is whether or not the incorporation of film effect in the pore-network models leads to a better agreement with experimental results. In this section, comparisons are made with two experiments performed using two different two-dimensional model

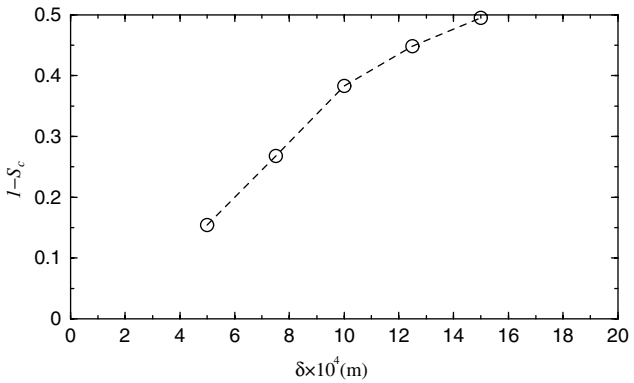

Fig. 10. Evolution of critical gas saturation $S_{gc} = 1 - S_c$ as a function of external transfer length scale δ.

porous media. In the first one, referred to as EXP1, an etched 100×60 square network initially fully saturated by Hexane is used. Except for the network size, the experiment is completely identical to the ones described in [13,14] (case $B = 0$). Therefore the details are not repeated here. One can also refer to [30] for additional details. The micromodel used for the second experiment, referred to as EXP2, is different and based on a random distribution of a 1 mm glass beads monolayer confined between two transparent glass plates. The beads are randomly thrown onto a glass plate coated with a sticky film. After removal of the excess beads a glass plate is put on top of bead monolayer. Then, three sides of this system are sealed by Plexiglas plates coated with Araldite®. The model is initially fully saturated by pure water. Vapour escapes through the open edge of model. The 12.2 cm long and 7.2 cm wide model is placed horizontally in a small transparent Plexiglas chamber of controlled temperature (22 ± 1 °C). The relative humidity in the chamber is stabilized using a LiCl saturated solution (RH $\approx$ 12%). The relative humidity and temperature near the open edge of model were recorded during the experiments using a sensor connected to a PC and no noticeable evolution was observed. Evolution of the model weight during drying is measured with a precision balance which is connected to the PC. Further details on this type of experiment can be found in [31].

3.4.1. EXP1

To perform the simulation we have to specify the network size (100×60), the lattice spacing (1 mm), the bond size distribution (we have taken a uniform distribution law with $R_{0\min} = 0.2$ mm and $R_{0\max} = 0.4$ mm), the fluid properties (hexane), the external length δ (we have taken $\delta = 1$ mm from the experimental data) and the geometrical and equilibrium properties associated with the fluid and the microstructure. For hexane on resin, the contact angle is very low and therefore it seems adequate to take $\theta = 0$. The shape of the duct cross-section in the micromodel is rectangular. It is therefore reasonable to take $N = 4$. However, with these inputs the simulation leads to a drying much faster than in the experiment (the simulation leads to sub-regime 1, i.e. a constant drying rate). This is attributed to a wrong representation of the hydraulic conductivity of the films within the micromodel. In the micromodel, there are corners and wedges in the bonds (that are ducts of rectangular cross-section) but not within the intersections of the network of ducts forming the pore space. In the intersections, the film connectivity is presumably due to smaller scale geometrical defects such as wall roughness [32]. As a result, our film model overestimates the hydraulic conductivity of the films. Considering that the corners form a connected sub-network is an unrealistic idealized view. In fact the film model should not be thought as based on a direct representation of pore space (even for etched square network, due to the intersections that break the corner continuity). The idea is rather to represent the effect of films in some average sense since it is very difficult to represent every nook and cranny in the pore space directly. From Eq. (20), it is clear that the details about the geometrical properties of the film sub-network are taken into account through the dimensionless factor f. Hence the question becomes: is it possible to adjust the value of f so as to obtain a satisfactory agreement with the experimental results? To this end, we are free to play with the contact angle and the number of sides N, which are the two parameters affecting f. Thus, in this context, the contact angle should not be viewed as representative of the physical contact angle but as a parameter controlling the overall transport properties of the film. As shown in Fig. 11, a good agreement is found with the experimental results with $N = 4$ and $\theta/\theta_c \approx 0.86$. These results confirm that incorporating the film effects is a necessary ingredient in the modelling. As can be seen from Fig. 11, the drying time is strongly overestimated when the film effect is neglected in agreement with previous simulations [14]. As pointed out in [8], the comparison illustrates the fact that the model represents a good approximation to the complicated problem of film flow in drying processes but also that the film sub-network geometry is too simplified for a direct prediction without adjusting f.

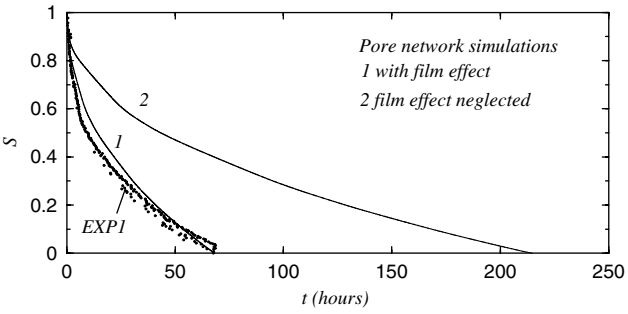

Fig. 11. Experimental and simulated drying curves (EXP1).

3.4.2. EXP2

The pore space corresponding to the micromodel used in EXP2 is quite different from the square network of polygonal capillaries corresponding to the etched network used in EXP1. Thus, here again, we simply expect that it is possible to adjust the dimensionless factor f so as to obtain an agreement with the experimental data much better than with the pore-network model ignoring the film effect. The simulation has been performed for a 122×72 network with a lattice spacing of 1mm and water as working fluid. The bond size distribution is uniform with $R_{0\min} = 0.3$ mm and $R_{0\max} = 0.5$ mm. The external length δ is determined by calibration from the experimental data in the first phase of drying. This gives $\delta \approx 1.5$ mm. As for EXP1, we have taken $N = 4$ (we could have taken $N = 3$ or 6, this would have led simply to a different value of the fictitious contact angle θ) and varied θ/θ_c in order to improve significantly the agreement with the experimental data. As shown in Fig. 12, a reasonably "good" agreement is obtained with

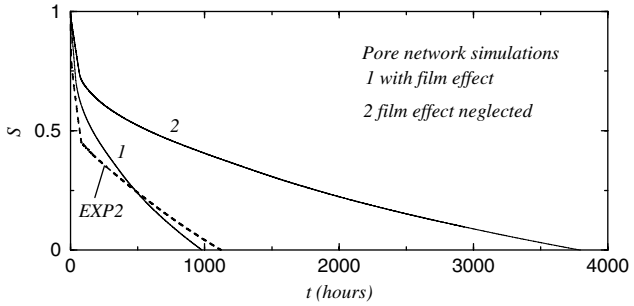

Fig. 12. Experimental and simulated drying curves (EXP2).

$\theta/\theta_c = 0.94$. It is interesting to note that this value is greater than the value used for the simulation of EXP1 ($\theta/\theta_c = 0.86$). This is consistent with the idea that the overall film hydraulic conductivity in a layer of beads is lower than in a network of ducts of rectangular cross-section since rectangular ducts favour the corner flows. Again, the comparison shows that neglecting the film effect strongly overestimates the drying time. The pore-network model with films leads to a much better agreement with the experimental data. However, the comparison is not as good as for EXP1, which is not surprising owing to the pore space geometry which is quite different from a square network of rectangular ducts. The drying curve of EXP2 presents some noticeable differences compared to the one of EXP1. In both experiments, one can distinguish two main drying periods, corresponding presumably to a progressive transition from sub-regime 1 to sub-regime 2. However, the transition is much sharper for EXP2. Furthermore, a closer look at the first period of EXP2 reveals that this period can be divided into two sub-periods of almost constant rate (this is hardly visible in Fig. 12 owing to the time axis scaling needed to represent the no film simulation results). This is not observed in EXP1 and not predicted by the pore-network model with films. This is an additional indication that the effect of liquid film is more subtle than predicted by the simplified model considered in this paper. Clearly, further work is needed to improve our understanding of film flows in drying processes.

4. Discussions

In agreement with the experiments reported in [14] and the simulations presented in [7], the simulations as well as the experiments presented in this paper confirm that film flows can dramatically affect the drying rate and lead to a much faster drying. As it has been shown, the influence of film flows is strongly dependent on contact angle and pore shape. The pore shapes considered in the present paper are very idealized and are not thought as direct representations of real porous media. The idea is rather to represent the effect of films in some average sense since it is very difficult to represent every nook and cranny in the pore space directly. However, our study indicates that drying rate can be very sensitive to these details of the pore space when conditions are such that film flows are important. This contributes to explain why the quantitative prediction of drying rates largely remains an open question as it has also been illustrated in the comparison with experimental data.

The constant rate period (CRP) is one of the most striking and puzzling feature of convective drying of capillary porous media. In two-dimensional systems with usual bond size random distributions, such a CRP cannot be observed in the absence of film for topological reasons (unless invasion percolation in a gradient (IPG) effects maintain high saturation at the surface of porous medium, see [6,9,14] for more details and the discussion below or special microstructures are considered [19]). As can be seen from our study, a simple bundle of non-interconnected polygonal capillary tubes can lead to a CRP owing to the film effect. Hence several mechanisms can contribute to the occurrence or the duration of the CRP, namely capillary effects associated with the distribution of (throats) size, IPG effects and film flows. As shown in [10], invasion percolation rules combined to diffusion transport in the gas phase are sufficient to obtain a CRP in 3D. In this case, the CRP is due to the fact that invasion of the gas phase take place in the largest throats (between R_{0c} and R_{0max}). As a result the saturation at the porous surface does not change appreciably over a significant period. In [10], a local mass transfer coefficient was used to take into account the external mass transfer. Thus the additional effect of water vapour homogenisation by lateral diffusion within the external boundary layer [33], was not taken into account in [10]. This effect can contribute to enhance the CRP predicted in [10], see [12] or [19]. As mentioned before and shown in [14], IPG mechanisms can also contribute to the occurrence and duration of CRP when they are destabilizing (IPDG). IPDG patterns can be induced by gravity effects [14], thermal gradient [6], or concentration gradients [9]. IPDG patterns are associated with a constant high saturation at the porous medium surface over a significant part of the invasion. This leads to a CRP induced by destabilizing gradients. As discussed in this paper, film flows can also lead to the occurrence of a CRP. The first mechanism associated with standard IP patterns leads to a CRP in 3D systems only whereas film flows and IPDG patterns can lead to a CRP in 3D and 2D systems. Here we do not consider the case where the external mass transfer length scale δ is much larger than the porous medium thickness since this case is not representative of classical convective drying. It is obvious that drying rates are quasi-constant in the limit $\delta \gg L$.

5. Conclusion

This article has reported an investigation of the effect of pore shape and contact angle during the isothermal drying of porous materials in relation with the effects of macroscopic liquid films when viscous effects are important in the films but not in the saturated pores. As discussed in

several previous works, these films can represent a major transport mechanism.

Several regimes have been identified. When the contact angle is above a certain critical angle, the films cannot develop and the transport in the invaded region of porous medium is only by diffusion. This situation leads to the slowest drying and the pore shape has little effect on the drying process. The opposite extreme situation is when the films extend up to the surface of porous medium during the whole drying. This leads to the fastest drying rate. The difference in the drying times between the internal vapour diffusion controlled drying and the dominant film flow regime can be very important (less than 4 days against more than 8 months for one of the particular examples considered in this study). The pore shape and contact angle have no effect on drying as long as the films do not recede within the porous material during drying. By contrast, both the contact angle and the pore shape greatly affect drying in the intermediate regime where films represent a major transport mechanism but recede within the porous medium during drying. Our results contribute to explain why the accurate prediction of drying rate of a porous medium can be a very challenging task since the drying rate may depend on somehow tiny details of the pore space geometry and is affected by possible changes in the local wettability conditions.

Film flows can lead to a constant rate period (CRP) even in two-dimensional systems. This has led to distinguish several mechanisms that can contribute to the occurrence of the CRP in drying: lateral transfers in the external mass boundary layer, film flows, IP and IPDG mechanisms.

As pointed out in [7], the film flow model we have used suffers from several limitations. In particular, the model does not take into account the possible intercluster transport by the films. This aspect would deserve to be investigated in details. What is more, pore shapes in a porous medium are clearly more complex than the straight tubes considered in this paper. In this respect, the film flow model used here should be understood as describing the effect of film flows in an average and qualitative sense only. This has been illustrated in the comparison with experimental data presented in this paper. Therefore further work is certainly needed to improve the modelling of film flows in drying processes.

Acknowledgement

I thank N. Sghaier for permission to use the experimental data corresponding to EXP2.

References

[1] M. Prat, Recent advances in pore-scale models for drying of porous media, Chem. Eng. J. 86 (1–2) (2002) 153–164.
[2] M. Prat, Percolation model of drying under isothermal conditions in porous media, Int. J. Multiphase Flow 19 (1993) 691–704.
[3] M. Prat, Isothermal drying of non-hygroscopic capillary-porous materials as an invasion percolation process, Int. J. Multiphase Flow 21 (5) (1995) 875–892.
[4] A.G. Yiotis, A.K. Stubos, A.G. Boudouvis, Y.C. Yortsos, A 2-D pore-network model of the drying of single-component liquids in porous media, Adv. Wat. Res. 24 (2001) 439–460.
[5] H.P. Huinink, L. Pel, M.A.J. Michels, M. Prat, Drying processes in the presence of temperature gradients. Pore-scale modelling, Euro. Phys. J. E 9 (2002) 487–498.
[6] F. Plourde, M. Prat, Pore network simulations of drying of capillary media. Influence of thermal gradients, Int. J. Heat Mass Transfer 46 (2003) 1293–1307.
[7] A.G. Yiotis, A.G. Boudouvis, A.K. Stubos, I.N. Tsimpanogiannis, Y.C. Yortsos, The effect of liquid films on the drying of porous media, AiChE J. 50 (11) (2004) 2721–2737.
[8] A.G. Yiotis, A.K. Stubos, A.G. Boudouvis, I.N. Tsimpanogiannis, Y.C. Yortsos, Pore-network modeling of isothermal drying in porous media, Transport Porous Media 58 (2005) 63–86.
[9] D.S. de Freitas, M. Prat, Pore network simulation of evaporation of a binary liquid from a capillary porous medium, Transport Porous Media 40 (2000) 1–25.
[10] Y. Le Bray, M. Prat, Three dimensional pore network simulation of drying in capillary porous media, Int. J. Heat Mass Transfer 42 (1999) 4207–4224.
[11] L.A. Segura, P.G. Toledo, Pore-level modeling of isothermal drying of pore networks. Effects of gravity and pore shape and size distributions on saturation and transport parameters, Chem. Eng. J. 111 (2005) 237–252.
[12] A.G. Yiotis, I.N. Tsimpanogiannis, A.K. Stubos, Y.C. Yortsos, Pore-network study of the characteristic periods in the drying of porous materials, J. Coll. Interface Sci. 297 (2006) 738–748.
[13] J.B. Laurindo, M. Prat, Numerical and experimental network study of evaporation in capillary porous media. Phase distributions, Chem. Eng. Sci. 51 (23) (1996) 5171–5185.
[14] J.B. Laurindo, M. Prat, Numerical and experimental network study of evaporation in capillary porous media. Drying rates, Chem. Eng. Sci. 53 (12) (1998) 2257–2269.
[15] I.N. Tsimpanogiannis, Y.C. Yortsos, S. Poulou, N. Kanellopoulos, A.K. Stubos, Scaling theory of drying in porous media, Phys. Rev. E 59 (4) (1999) 4353–4365.
[16] M. Prat, F. Bouleux, Drying of capillary porous media with stabilized front in two-dimensions, Phys. Rev. E 60 (5) (1999) 5647–5656.
[17] T.M. Shaw, Drying as an immiscible displacement process with fluid counterflow, Phys. Rev. Lett. 59 (15) (1987) 1671–1674.
[18] A. Irawan, T. Metzger, E. Tsotsas, Pore network modeling of drying: combination with a boundary layer model to capture the first drying period, in: 7th World Congress of Chemical Engineering, Glasgow, Scotland, 2005.
[19] T. Metzger, E. Tsotsas, M. Prat, Pore network models: a powerful tool to study drying at the pore level and understand the influence of structure on drying kinetics, in: A. Mujumdar, E.T. Tsotsas (Eds.), Chapter 2 in "Modern Drying Technology", Vol. 1 "Computational Tools at Different Scales", Wiley, in press.
[20] J. Van Brakel, Mass transfer in convective drying, in: A.S. Mujumdar (Ed.), Advances in Drying, Hemisphere, New York, 1980, pp. 217–267.
[21] S. Jin, K.S. Breuer, Diffusion-limited evaporation in long microchannels, in: Proceedings of IMECE03, 2003 ASME International Mechanical Engineering Congress and Exposition, Washington, DC, USA, 16–21 November 2003.
[22] B. Camassel, Contribution à l'étude du changement de phase liquide vapeur en milieu poreux, Ph.D. thesis, INPT, 2003.
[23] B. Camassel, N. Sghaier, M. Prat, S. Ben Nasrallah, Ions transport during evaporation in capillary tubes of polygonal cross section, Chem. Eng. Sci. 60 (2005) 815–826.
[24] T. Coquard, B. Camassel, M. Prat, Evaporation in capillary tubes of square cross section, in: Proceedings of HT2005, 2005 Summer ASME Heat Transfer Conference, San Fancisco, CA, USA, 17–22 July 2005.
[25] R.B. Bird, W.E. Stewart, E.N. Lightfoot, Transport Phenomena, Wiley, New York, 1960.

[26] H. Wong, S. Morris, C.J. Radke, Three dimensional menisci in polygonal capillaries, J. Coll. Interface Sci. 148 (2) (1992) 317–336.
[27] G. Mason, N. Morrow, Meniscus curvatures in capillaries of uniform cross-section, J. Chem. Soc. Faraday Trans. 1 80 (9) (1984) 2375–2393.
[28] T.C. Ransohoff, C.J. Radke, Laminar flow of wetting liquid along the corners of a predominantly gas-occupied noncircular pore, J. Coll. Interface Sci. 121 (1988) 392–398.
[29] D. Zhou, M. Blunt, F.M. Orr, Hydrocarbon drainage along corners of noncircular capillaries, J. Coll. Interface Sci. 187 (1997) 11–21.
[30] J.B. Laurindo, Evaporation en milieu poreux, Etude expérimentale sur milieux-modèles et modélisation de type percolation, INPT Ph.D. thesis, Toulouse, France, 1996.
[31] N. Sghaier, Evaporation en milieu poreux en présence de sel dissous, Influence des films liquides et des conditions de mouillabilité, Ph.D. thesis, INPT, 2006.
[32] R. Lenormand, C. Zarcone, Role of roughness and edges during imbibition in square capillaries, SPE 13264, 1984.
[33] M. Suzuki, S. Maeda, On the mechanism of drying of granular bed-mass transfer from discontinuous source, J. Chem. Eng. Jpn. 1 (1) (1968) 26–31.